AI-based Risk Assessment for Construction Site Disaster Preparedness through Deep Learning-based Digital Twinning

Mirsalar Kamari[1] and Youngjib Ham, Ph.D.[2]

[1] PhD Candidate, Department of Construction Science, Texas A&M University, 3137 TAMU, College Station, TX 77843; PH (979) 446-9385; email: kamari@tamu.edu

[2] Associate Professor, Department of Construction Science, Texas A&M University, Francis Hall 329B, 3137 TAMU, College Station, TX 77843; PH (979) 458-0184; email: yham@tamu.edu

Abstract

Hurricanes are among the most devastating natural disasters in the United States, causing billions of dollars of property damage and insured losses. During extreme wind events, unsecured objects in jobsites can easily become airborne debris, which results in substantial loss to construction projects and neighboring communities. Toward a systematic disaster preparedness in construction jobsites, this paper presents a novel vision-based digital twinning and threat assessment framework. We encode the context of disaster risk into deep-learning architectures to identify and analyze the characteristics and impacts of potential wind-borne debris in construction site digital twin models. Case studies on nine piles of construction materials are presented to demonstrate and discuss the fidelity of the proposed computational modules. The proposed methods are expected to help provide heads up for practitioners to quickly recognize, localize, and assess potential wind-borne derbies in construction jobsites, and thereby implementing hurricane preparedness in an effective and timely manner.

1. Introduction

Dynamic and complex construction sites including incomplete structures and unsecured resources, are among the most vulnerable environments to extreme wind events [1]. Severe wind-induced damages significantly attenuate the efficiency of construction projects by causing considerable schedule delays and further negatively impact neighboring infrastructures in operations (e.g., roads, power grids), and thus trigger notable disruptions and financial losses in communities [1,2]. For instance, along with around 50 billion dollars in damage and more than 250 fatalities, Hurricane Sandy has caused over 185 million dollars' worth of damage to the construction project of the World Trade Center [3,4]. Severe wind-induced disruptions could be classified in three folds: (1) structural or mechanical failures such as tower crane collapses due to excessive wind loads [5-7]; (2) functional failure such as the inability to make progress due to construction suspension and supply chain disruption before and after extreme weather events [8]; and (3) (cascading) damages due to the devastating impact of potential wind-borne debris that is imposed to construction sites (as well as neighboring communities including critical infrastructure systems) [9,10]. The wind-borne debris in construction sites pose a substantial risk as unsecured resources could easily become projectiles during extreme wind events, and cause mass casualty incidents or induce damages to critical infrastructure systems in operation [1,11,12]. For example, eyewitness accounts indicate a total loss of 7.5 million dollars in damage to the four-story hotel construction site in Batavia, IL due to the aftermath of an extreme wind event [13]. Additionally, the charlotte county in Miami, FL has warned that unsecured construction materials such as plywoods and portable toilets in jobsites are among the most common projectiles in the case of extreme wind events [14]. Local contractors in the charlotte harbor area pointed out that they need to effectively remove loose materials and tie them down as the impact of such debris to the neighboring communities would be substantial [15]. Meanwhile, according to a report from the United States Department of Homeland Security, an estimated cost for hauling and removal of 200,000 cubic yards of debris for Hurricane Irma was estimated at around 1.4 billion dollars [15,16]. The majority of the debris was classified as construction-related materials or vegetation that became airborne during hurricanes, and it is noted that the associated hauling process took several months to complete by the local government [15].

While concurrent building codes and ordinances support designing wind-resilient structures with respect to severe weather conditions, construction companies are responsible for regulating and implementing hurricane preparedness plans to better protect their projects during construction phase [2]. Preparedness plans involve a list of activities that are geared towards mitigating wind-induced damage in projects [17], and such emergency operating procedures are typically based on the experiences and expertise of practitioners in companies. Also, in order to implement the preparedness plans before hurricanes, practitioners need to perform visual inspections to identify potential risks based on checklists. However, their manual inspection to recognize threats in jobsites could be error-prone and labor-intensive [18], and thus it is expected that the quality of practitioner’s efforts to mitigate the impact of wind-induced damages to be likely degraded in a limited timeline for preparedness of large-scale jobsites.

Meanwhile, over the years, emerging technologies in visual sensing and analytics have demonstrated a great potential to streamline the management task of practitioners in construction projects [19-26]. For example, the convenience of commercial-level unmanned aerial vehicles (UAVs) encourages practitioners to collect large-scale visual data to keep the as-is record of construction sites [20,21,27]. In addition to images from the ground level, aerial imagery collected from UAVs can provide an overhead view of resources in jobsites, which can assist with surveying and mapping [28], progress monitoring [29-32], and safety management [33-35]. In the context of hurricane preparedness in construction sites, UAVs have demonstrated the potential to capture an invaluable record of potential wind-borne debris from aerial vantage points [1]. Exploring through imagery would provide critical information regarding the type and location of potential threats, allowing practitioners such as safety directors and superintendents to better prepare and implement emergency operating procedures to secure jobsites prior to extreme weather events.

In this paper, we propose a novel vision-based framework for construction site hurricane preparedness. By leveraging visual data from jobsites, we reconstruct a digital twin model of the at-risk construction environment that recognizes the type and the location of threats at the 3D level. In this regard, we first perform an image-based scene reconstruction, and then carry out the semantic segmentation on images to identify potential wind-borne debris at the 2D level. Building on the outcome of the 2D sematic segmentation, we project the semantic values onto the point cloud model to obtain the semantic information of potential wind-borne debris at the 3D level. Finally, for each instance of potential wind-borne debris, we estimate the associated quantity and assess the inherent threats based on the kinetic energy. A site-specific heat map is generated to delineate the risk associated with potential wind-borne debris with respect to the severity of given wind events. We evaluated the performance of the proposed methods on residential construction sites in College Station, TX, especially those associated with wooden dwellings where unstructured resources such as pine boards and plywoods are found. The proposed framework will help practitioners to effectively locate potential wind-borne debris in construction sites and understand the associated risk. Thus, it can support risk-informed decision-making by providing heads-up to practitioners in a timely fashion, which fosters awareness of the ways in which hurricanes cloud be destructive in construction sites.

2. Research Background

2.1. Disaster preparedness and potential wind-borne debris

Prior works on post-disaster management are geared towards activities based on the severity of damage after disaster strikes in given regions [36,37]. In contrast, pre-disaster management focuses primarily on the adaptation of mitigation and preparedness plans through a proactive risk assessment [38]. In this regard, Gregg et al. [39] carried out preemptive risk assessment building on the geographic location of given regions and the distance to hazard-prone areas, past experiences, and the probability of potential future incidences. According to [40], for every 2.5 dollars investment in pre-emptive efforts and practices in disaster management, a one-hundred-dollar bill can be saved by reducing the cost of disaster-related losses. Although the related contexts would differ, such study infers the significance of proactive practices and studies to identify threats and mitigate the potential impact of disasters in construction jobsites.

In order to implement preparedness practices, practitioners such as safety directors or superintendents should first recognize potential threats in jobsites [41]. If not properly recognized, preemptive efforts are likely subjected to failures [41,42]. Interestingly, demographic variables such as education and training of practitioners may impact the extent to which proactive efforts are adapted [43,44]. In this regard, technology-driven studies (e.g., eye-tracking) have been conducted for the cognition of hazards among practitioners in construction sites [18,45-47]. The general concept of these studies is to assess the quality of practitioners' visual search to recognize deficiencies, which can help better educate practitioners to flag and perceive potential threats in jobsites [48,49]. Although such works demonstrate the great potential in identifying the location of hazards in construction sites, when it comes to visual inspection on potential wind-borne debris, there is an additional need to consider the geometrical characteristics (e.g., shape, volume) that needs to be further assessed to better understand the associated risk. To this end, such studies on hazard detection would not be expected to directly translate into desirable outcomes in assessing the extent of threats in the context of potential wind-borne debris.

Meanwhile, studies have been carried out to characterize the behavior of general wind-borne debris. [10] evaluated potential damage of wind-borne debris to building envelopes with respect to the severity of wind events. Later, [50] classified the shape of wind-borne debris into three categories (compact, plate, and rod) as each shape demonstrates different behaviors in severe wind events. Building on the geometrical characteristics, [51,52] studied possible trajectories of rod and sheet type of debris in severe wind events. As such, a systematic foundation to quantify the extent of damage with regards to types and shapes of potential wind-borne debris has been established. Building on these, we propose a vision-based framework to automatically identify and assess threats of potential wind-borne debris in construction sites. The proposed framework for scene understanding is essential to support the localization of potential threats in construction sites and prioritization for preparedness planning. As a point of departure, in the following section, we review the research on scene understanding focusing on point cloud segmentation.

2.2. Digital twining and point cloud segmentation

3D scene understanding such as point cloud segmentation is a rising field of study that has a wide range of applications such as robotics [53], augmented reality [54], autonomous driving [55], and medical imaging [56]. The objective of scene understanding is to cluster points belonging to a specific object in point cloud models. In order to better process 3D data, prior works represent the point cloud models in the context of multi-view images [57], voxels [58], and meshes [59]. Such methods help the classification of points belonging to a target class, but not the instance segmentation for objects in a particular class. Moreover, the conversion of point cloud models to voxels and mesh representations is likely subjected to data loss, which may lead to poor performance in classification [60]. In this regard, [60] adopted a deep learning framework, referred to as PointNet, which directly uses point cloud data as the preliminary input. PointNet framework was the first to address point permutations, and the extracted deep-learning descriptors are robust to order invariances in the 3D point cloud. Despite the benefits of PointNet, one of the challenges is that a relatively small number of points (e.g., 1024, 2048, 4096) can be processed by its workflow due to the fixed size of the input layer of the deep neural networks. To this end, the process of semantic segmentation and scene parsing of point cloud models containing millions of points (e.g., reconstructed scenes of large-scale jobsites) has been identified as a challenge for PointNet architecture.

In the construction domain, prior works on point cloud segmentation could be divided into model-driven and data-driven frameworks [61]. Model-driven segmentation of point clouds enables the classification of points based on a set of hand-engineered cost functions such as in shape-fitting algorithms or region-growing workflows. In this regard, [62] proposed a method to address the segmentation of 3D point clouds of bricks in masonry walls, and [63] performed the segmentation of infrastructures based on region-growing algorithms. Later, [64] carried out the automatic detection of safety regulation compliances (e.g., toe-boards) on point cloud data. Despite the benefits of such models (e.g., computational simplicity), insufficient robustness to geometrical variances and poor performance on noisy and incomplete point cloud models have been identified as the limitation of model-driven point cloud segmentation frameworks [61]. On the other hand, data-driven models rely on diverse training datasets to categorize points in point cloud models. In this regard, studies such as [65] have addressed point cloud segmentation through the supervised learning. For instance, [66] addressed the detection of scaffolding in point clouds through the Random Forest framework. Studies were performed for the categorization of planner patches [67] (e.g., columns, beams, slabs) and rebars [68] in laser scanning data using conventional classification approaches such as support vector machine (SVM). Later, [69] addressed the segmentation and classification of construction machinery in 3D laser scanning models, building on a descriptor using a synthetic training dataset. Despite the potentials, there is still a challenge in the application of synthetic data due to the limited capacity in representing textural and geometrical variances of real-world point cloud models [70], which needs further studies. Other studies have carried out 3D level segmentation building upon the projection of 2D semantic values onto the point cloud model for material piles [71] and construction equipment [38]. However, a limited 3D segmentation accuracy has been reported once 2D semantic information is projected onto point cloud models. In this regard, [71] implemented an elevation-based criterion to improve the performance of 3D semantic segmentation. Despite the performance enhancement, the elevation-based criterion is typically valid on flat surfaces, and thus its application to jobsites that often involve uneven surfaces would be challenging. To address the challenges, we propose a novel 3D semantic segmentation building on depth information, in order to robustly recognize potential wind-borne derbies from point cloud models.

3. Proposed Methods for Vision-based Construction Site Hurricane Preparedness

In this paper, the risk assessment on potential wind-borne debris (PWDs) using visual data is composed of three modules: 1) digital twinning of PWDs in jobsites based on collected visual data, 2) estimating the quantity of PWDs through the volumetric measurement, and 3) assessing the associated threats of PWDs with respect to the intensity of wind events. Case studies on nine piles of PWDs were conducted in residential construction sites to assess the fidelity of the proposed methods.

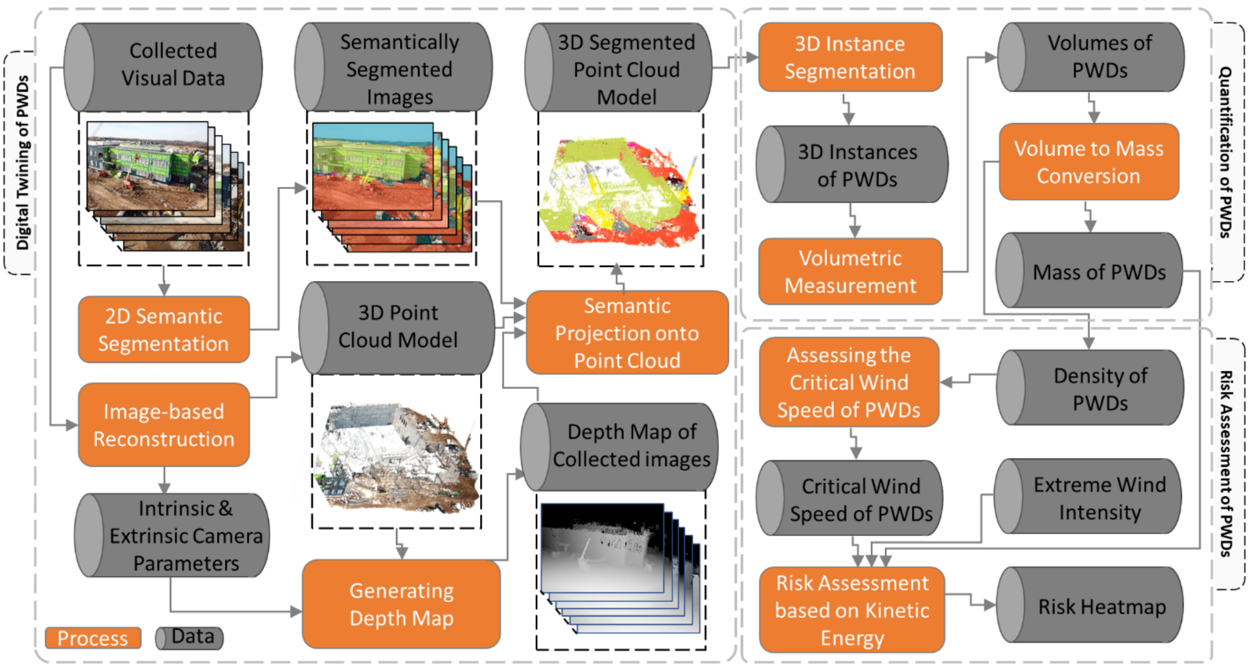

Figure 1. Overview of the proposed method for construction site hurricane preparedness using visual data

3.1. Digital twinning of construction sites including potential wind-borne debris

Digital twinning is a crucial step in representing the geometrical characteristics such as the shape and location of physical assets in a corresponding virtual environment [72]. In order to build a digital twin model, a 3D dense point cloud is first reconstructed using collected images. Building on Structure-from-Motion (SfM) [73] and Multi-View Stereo [74], a dense point cloud model represents a replica of construction sites including PWDs. The SfM framework could briefly be described as: 1) extracting a local feature descriptor such as Scale-Invariant Feature Transform (SIFT) [75] from entire images, 2) performing pairwise matching among feature descriptors of images to compute the fundamental matrix and obtain camera viewpoints (e.g., position and orientation) from where the data collection is performed, and 3) using triangulation to estimate the location of successful pairwise matches in a 3D coordinate system to obtain a sparse point cloud model. Subsequently, in order to populate the sparse point cloud, the Multi-View Stereo workflow is employed among collected images, which initially divides images into patches and enforces an iterative match, expand and filter procedures to refine the point cloud resolution [74]. Upon reconstruction of point cloud models of jobsites, the detection of PWDs and the associated analysis is performed.

3.1.1. Detection of PWDs

Most residential buildings in the United States, including those located in hurricane-prone regions, are wooden dwellings [76]. This implies that not only these wooden structures are susceptible to hurricanes, but also residential construction sites for such dwellings accommodate a large number of loose and easy-to-airborne PWDs (e.g., plywoods, pine boards) that are vulnerable to extreme wind events [77]. Depending on behaviors in severe wind situations, PWDs are classified into three types (rod, plate, and compact). The rod-type debris or linear debris is one-dimensional debris as one dimension is extensively larger than two others. Examples of the rod-type debris are wooden framing members or piping. The plate-type debris is known as planer debris, where one dimension is notably smaller than the other two dimensions. Pine boards or roof sheathing are examples of this type. Finally, the compact-type debris is referred to as three-dimensional debris, where its size in three dimensions is approximately similar, such as bricks. Table 1 summarizes common PWDs in residential construction sites.

Table 1. Examples of potential wind-borne debris (PWD) in construction sites

PWDs	**Debris Type [50]**
Bricks [77]	Compact-type
Roof surfacing [77]	Plate-type
Framing members [2,77]	Rod-type
Sheetrock [2,77]	Plate-type
Pine board [2,77]	Plate-type
Trash [77]	Compact-type
Piping [77]	Rod-type
Scaffolding Systems [2]	Rod-type
Roof Sheathing [77]	Plate-type
Roof trusses [77]	Rod-type
Shingles [2,77]	Plate-type

In order to detect PWDs in visual data, we leverage convolutional neural networks to perform semantic segmentation over images from construction sites. The semantic segmentation enables the categorization of pixels into semantic classes and specifies the boundaries of the objects of interest, paving the way to carry out the scene understanding [38,78]. We benchmarked the detection of PWDs based on different convolutional neural network architectures and presented the outcomes in the case study and evaluation section. Upon detecting PWDs in images, their geometrical characteristics such as dimension and type of debris and the unit weight are encoded for each class of PWD. The geometrical characteristics of PWDs are the critical information to specify their vulnerability with respect to the intensity of given wind events.

3.1.2. Point cloud segmentation to analyze PWDs in 3D

Building on 2D semantic segmentation, we perform point cloud segmentation to analyze PWDs in 3D (e.g., volume). For the point cloud segmentation, we establish a correspondence between the pixels of semantically segmented images and points in point cloud model. Such correspondence indicates what semantic pixel is associated with which point in point cloud models. Using camera viewpoints and extrinsic parameters obtained from the SfM, 2D pixel to 3D point correspondence between images and point cloud models is expressed as follows [71]:

$$C_i = K_{3\times3}[R_{3\times3}|T_{3\times1}]C_w \quad (1)$$

where C_i represents the pixel location in the segmented image, such as in $[x_i, y_i, 1]^T$, and C_w is its corresponding location in the 3D point cloud, such as in $[x_w, y_w, z_{w,} 1]^T$, K encapsulates the intrinsic camera parameter (e.g., focal length, distortion). R and T are the extrinsic camera parameter denoting the orientation and location of cameras with respect to the coordinate system of the point cloud. Figure 2 demonstrates a point cloud model obtained via collected images and examples of semantic segmentation outcomes. Building on Equation (1), single-camera projections are shown in Figure 3a. Equation (1) holds for all camera positions and viewpoints, and, when multiple cameras are projected onto the point cloud model, the most common semantic class among projection cameras is assigned to points in the point cloud model. Such collective decision-making on the semantic class of a point is required as the class of their corresponding pixels among projection cameras is not typically consistent among points [71]. Figure 3c represents the outcome of the semantic projection from all cameras.

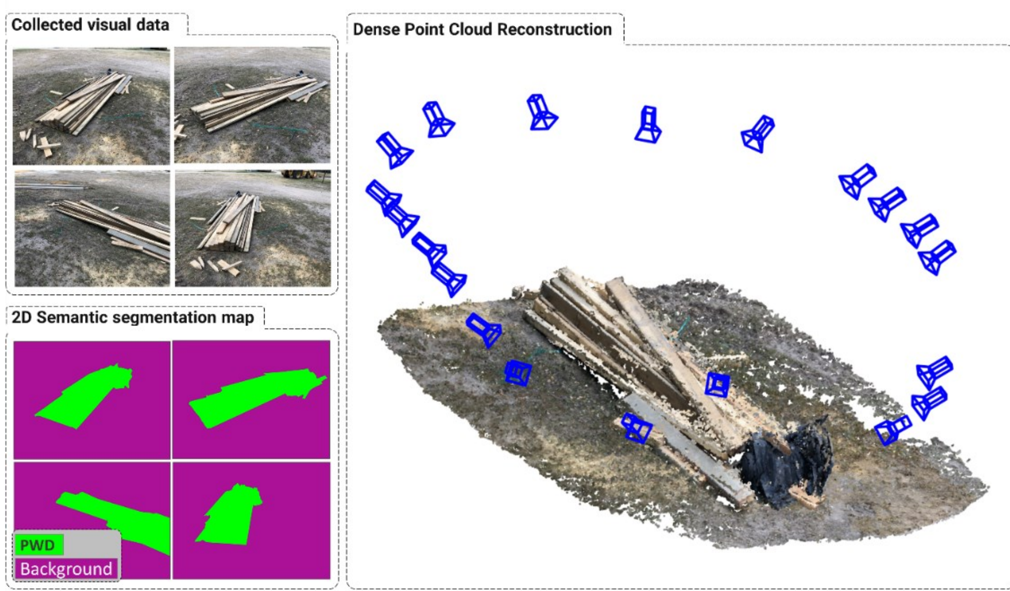

Figure 2. Examples of collected visual data, semantic segmentation, and camera viewpoints with respect to point cloud models

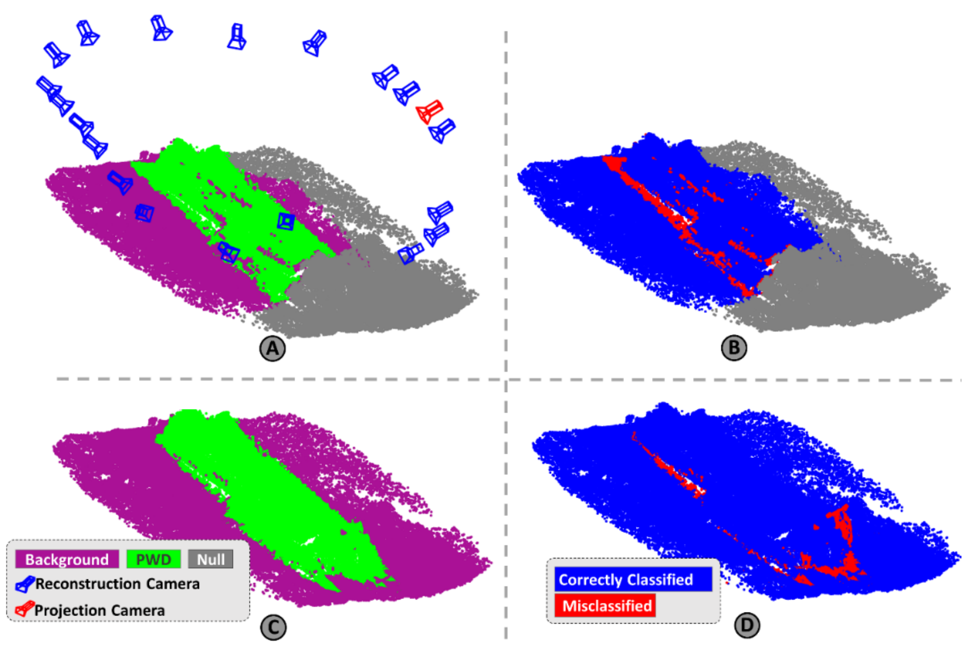

Figure 3. Semantic projection of single and multiple camera projections (A and C, respectively) and the classification confusion (B and D)

As observed in Figure 3b and 3d, 3D semantic segmentation through the camera projection is likely defective as parts of the background could be misclassified as PWDs. In particular, occluded objects could be misclassified since projection shadows are not taken into account in Equation (1), which leads to erroneous 3D segmentation outcomes. In order to improve the 3D segmentation by addressing the challenges, we propose the depth-aware projection framework. Building on the dense point cloud model, we compute a depth map at each camera location and use the depth information to take into account a range of projection. In this regard, given camera location and orientation, we render the viewpoint from the point cloud model where the camera is positioned and associated image is collected from (Figure 4a and 4b). We then divide the viewpoints into a grid of pixels (Figure 4c), and retrieve points in the point cloud model that are visible at each grid through the 2D pixel to 3D point correspondence between the image and the point cloud model. The distance of the closest point to the camera is retrieved at each grid location, and the depth map is generated accordingly (Figure 4f).

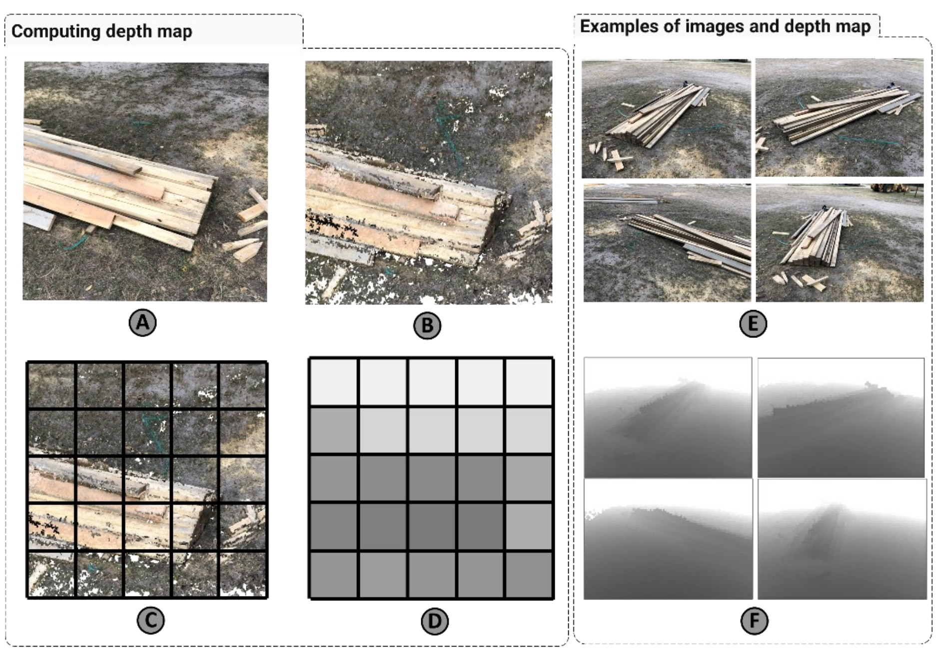

Figure 4. Overview of the proposed framework to compute depth maps from point cloud models

The distance demonstrated in the depth map accounts for the validity of Equation (1) during the semantic projection. In other words, at each grid location of the depth map, the semantic projection from image to point cloud may not be valid when points are located beyond the distance inscribed by the depth information. Figure 5 illustrates the performance enhancement through the proposed depth-aware projection framework. Figure 5a represents the projection without taking account of the depth information, which solely relies on Equation (1), and Figure 5b illustrates the depth-aware projection in which the background object is excluded from the semantic projection.

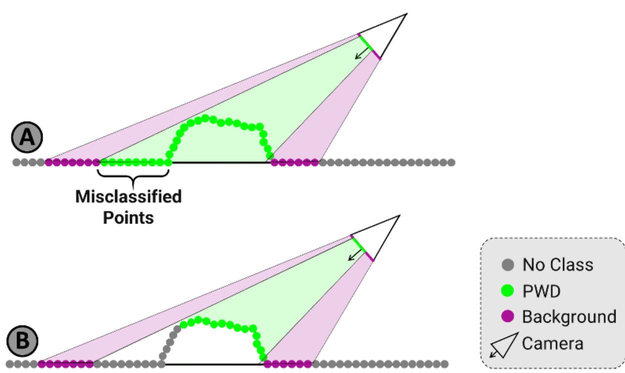

Figure 5. Illustration of the proposed depth-aware projection of semantic information onto point cloud models

The depth-aware semantic projection is the backbone of the proposed reality capturing of PWDs using visual data. Using the outcome of the 3D semantic segmentation, we further explore the characteristics of PWDs in the context of threats caused by extreme wind events.

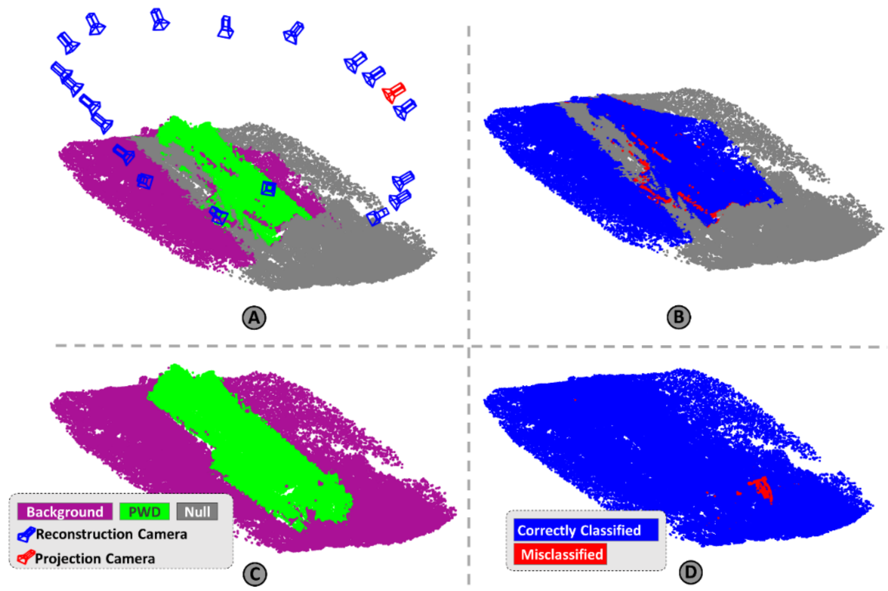

Figure 6. Depth-aware projection for enhanced 3D semantic segmentation

3.2. Estimating the quantity of potential wind-borne debris

The potential damage from PWDs is relevant to their weight, once they become projectile and collide into surrounding environments [50,77,79]. The associated collision damage is also referred to as the missile impact, which could be lethal to people who are in the immediate vicinity of PWDs during extreme wind events [79]. Generally, the higher the weight of PWDs, the greater the devastating impact is expected to take place during extreme wind events [50]. Using the outcomes of the point cloud semantic segmentation, we perform the volumetric measurement on PWDs, and then by using the unit weight values, we estimate the weight of PWDs. The volumetric measurement in the segmented point cloud model is composed of three modules as registration, projection, and resampling. Given segmented point cloud models, the Random Sample Consensus (RANSAC) algorithm [80] is employed for the ground registration through plane fitting [71]. Next, the point cloud model is demonstrated in the cartesian system in which its XoY plane lays over the registered ground, and its Z axis is parallel to the projection direction (Figure 7a). A grid of pixels over the registered ground is formed, and at each pixel location, a set of points enclosed within each grid is discretized. At each pixel location, the most common semantic class observed among points are inherited by the associated pixel as shown in Figure 7b. The outcome of such 3D to 2D projection is referred to as projection matte in this research.

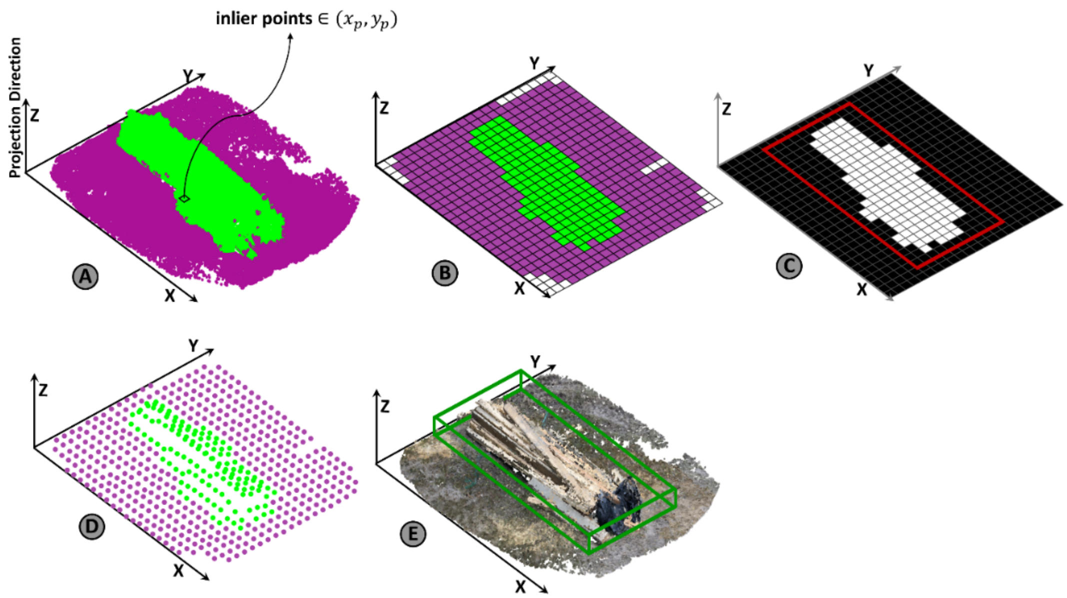

Figure 7. (a) segmented point cloud, (b) 2D projected matte, (c) instance segmentation, (d) resampled point cloud, (e) 3D bounding box

Upon the existence of multiple PWDs within a point cloud model, the instance segmentation of each PWD is required to separately assess their characteristics. In order to differentiate the instance of PWDs, a 2D bounding box is retrieved building on the projection matte, and the set of points enclosed within the bounding box is considered as a single instance (Figure 7c). At each pixel location of the projection matte, points representing the pixel are discretized, and the average Z height of points enclosed in each pixel is computed to obtain the resampled point cloud model (Figure 7d). To model the 3D bounding box containing the PWD, we build on the coordinates of the 2D bounding box and compute the maximum and minimum Z height values of the instance (Figure 7e). Finally, the volume of the PWD is computed as the summation of Z height values of the resampled point cloud model multiplied by the square size of pixels in the projected matte, which can be demonstrated as follows:

$$V_{pwd} = GS^2 \times \sum_{i=1}^{n} \sum_{j=1}^{m} Z_{pwd}((X_i, Y_j)) \tag{2}$$

where, V_{pwd} indicates the volume of PWD, Z_{pwd} is the height of points belonging to the PWD at the pixel location (X_i, Y_j), and the parameter GS denotes the grid size. The number of pixels of the projected matte in OX and OY directions are denoted as n and m. Building on the weight per unit volume of PWDs (which also referred to as the unit weight or special weight), the weight of PWDs is obtained as follows:

$$M_{pwd} = V_{pwd} \times \boldsymbol{\rho}_{pwd} \tag{3}$$

where M_{pwd} is the weight, and $\boldsymbol{\rho}_{pwd}$ is the unit weight of PWDs, respectively. Information regarding the unit weight of materials including PWDs, is generally available among practitioners, which enables them to plan for material transportation based on the weight or volume restrictions of transporting vehicles. Contractors also estimate the unit weight when purchasing materials or transporting materials and debris from one location to another.

3.3. Threat assessment of potential wind-borne debris

The possible damage imposed by PWDs is associated with its kinetic energy once it is picked up by wind and becomes airborne. Thus, to assess the threat in the context of PWDs, we calculate the kinetic energy associated with PWDs once they become projectiles. Basically, the kinetic energy of an airborne PWD is proportional to its mass and the square of its velocity, which is expressed as follows:

$$KE = \frac{1}{2} m_{pwd} U^2 \tag{4}$$

where KE indicates the kinetic energy of PWD (joules), m_{pwd} denotes the mass of PWD (kg) which is quantified in the section 3.2. The parameter U is associated with the intensity of the wind events and denotes the sustained wind speed (m/s). Not all PWDs become projectiles in wind events; some become projectiles at lower wind speeds, and some at a higher. Thus, the existence of projectiles is based on the critical wind speed. Such critical wind speed accounts for the minimum wind speed that is required to lift a PWD from the ground and make it a projectile [50]. Building on [50], the critical wind speed for different types of objects are expressed through Equation (5) and (6) as follows:

$$Uc^2 = 2\left(\frac{\rho_m}{\rho_a}\right)\left(\frac{I}{C_F}\right) lg \tag{5}$$

$$Uc^2 = \frac{\pi}{2}\left(\frac{\rho_m}{\rho_a}\right)\left(\frac{I}{C_F}\right) dg \tag{6}$$

where Uc denotes the critical wind speed of PWD, ρ_m denotes the weight to the volume of PWD, and ρ_a is the density of the air (kg/m^3). For the plate-type of PWD, l denotes its thickness, and similarly, d denotes the external diameter for the rod-type of PWD. The gravitational acceleration is denoted by g (m/s^2). The parameters I and C_F represent the bound and drag coefficient of PWD, which are assumed as unity in this research. By leveraging the mass and the critical wind speed, a heap map is generated to demonstrate threats associated with PWDs at a given wind speed. The heatmaps could be described as weighted pixels [81]. Here, at each pixel location, a weight is computed such that it satisfies Equation (4), provided that the given wind speed is greater than the critical wind speed of given PWDs.

4. Case Study and Evaluation

4.1. Data collection and experimental setup

In this research, two case studies were performed to evaluate the performance of the proposed method. Case #1 represents the laydown yard of a wooden residential construction site, while case #2 demonstrates a more complex jobsite of a commercial facility. There are nine piles of PWDs at different locations of the site (Figure 8a). There are three piles of pine board and plywood, two piles of PVC pipe, and a single pile of galvanized pipe. Case #2 consists of eight piles, including a single pile of sewer pipe, a single pile of metal pipe, a single pile of wooden boards, and five piles of steel beams at different locations (Figure 8b)

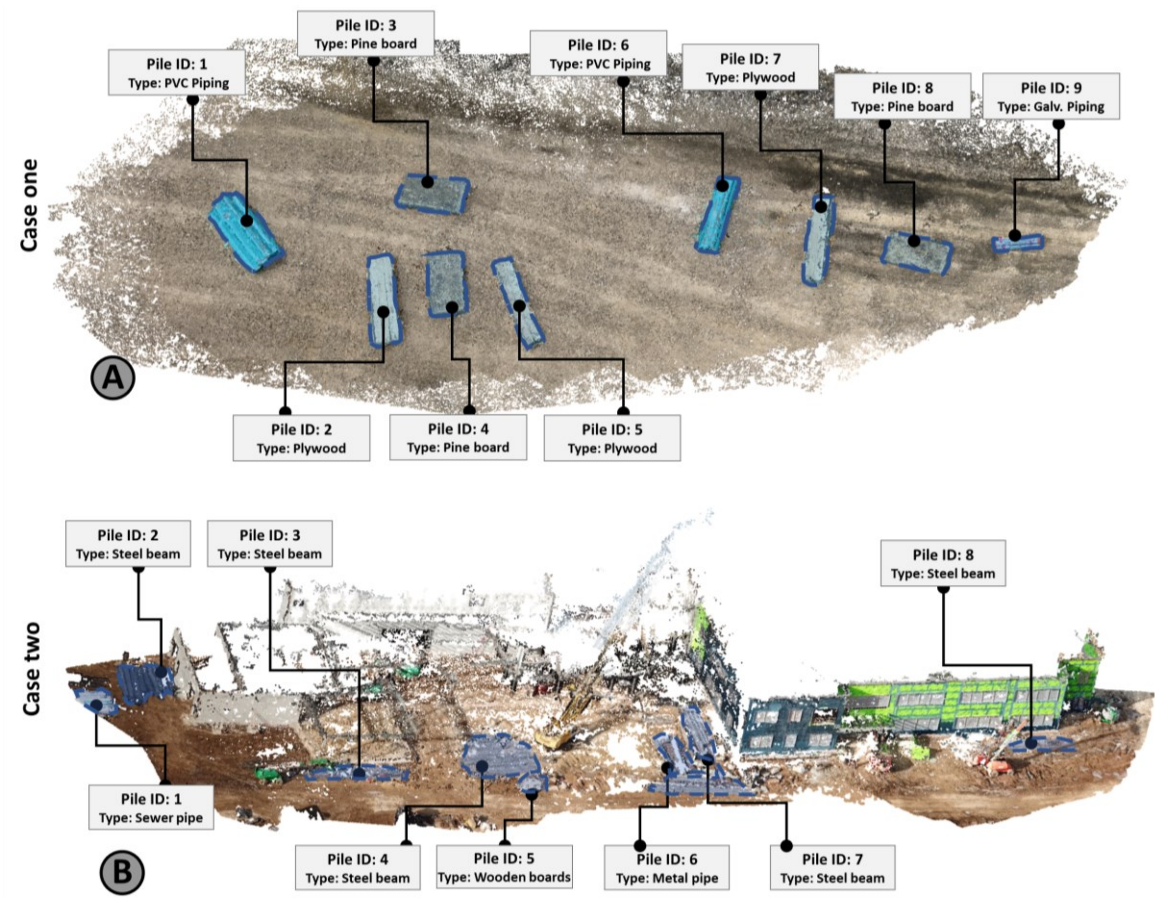

Figure 8. Types and locations of PWDs in case studies

The training dataset in case #1 consists of 360 images (180 from aerial perspectives and 180 from ground-level). In addition to the aerial visual data collection, due to the proliferation of hand-held camera-equipped platforms such as smartphones and tablets, ground-level visual data collections are also considered as the convenient way by practitioners to keep the record of the as-is status of the jobsite (e.g., prior to extreme weather events such as hurricanes for the purpose of insurance claim afterward). In order to demonstrate the robustness of the algorithm to both aerial and ground-level image, the semantic segmentation network was trained and tested on images from these two domains. In this regard, to evaluate the performance of the network, a total of 60 images, consisting of 30 aerial and 30 ground-level images, were randomly selected as the testing dataset. In case #1, aerial images were collected from a mid-end commercial UAV which is equipped with a 12-megapixel camera with a 35 mm lens and ISO range of 100-1600. Flight altitude was around 10 meters with respect to the ground, and the total flight time was around 3 minutes. Ground-level images were collected from a smartphone with a 12-megapixel camera at around 1.5 meters above the ground. In case #2, 32 aerial images were used for scene reconstruction in the form of point clouds and to assess the performance of the semantic segmentation. A total number of 127 images were used to train the semantic segmentation framework. The aforementioned UAV has been used for aerial visual data collection. The flight time was around two minutes, and the flight altitude was approximately 30 meters. Figure 9 shows the collected data in case studies and their corresponding segmented images and depth maps.

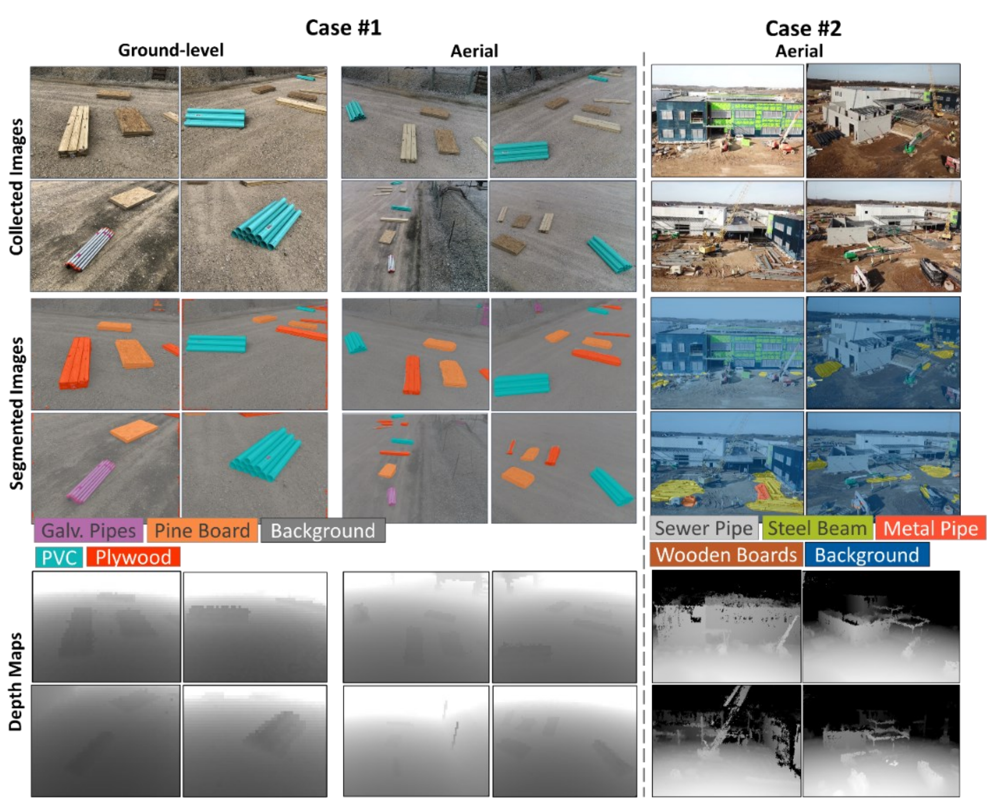

Figure 9. Examples of collected images, segmented images, and their associated depth maps in case studies

4.2. Performance metrics and outcomes

4.2.1. Semantic segmentation

The boundaries of PWDs are manually labeled to train the semantic segmentation model, as shown in Figure 10. In order to carry out the semantic segmentation at the 2D level, we built upon different architectures of convolutional deep neural networks, including Alexnet [82], Vgg19 [83], Resnet18 [84], and Resnet50 [84], and evaluated their performance.

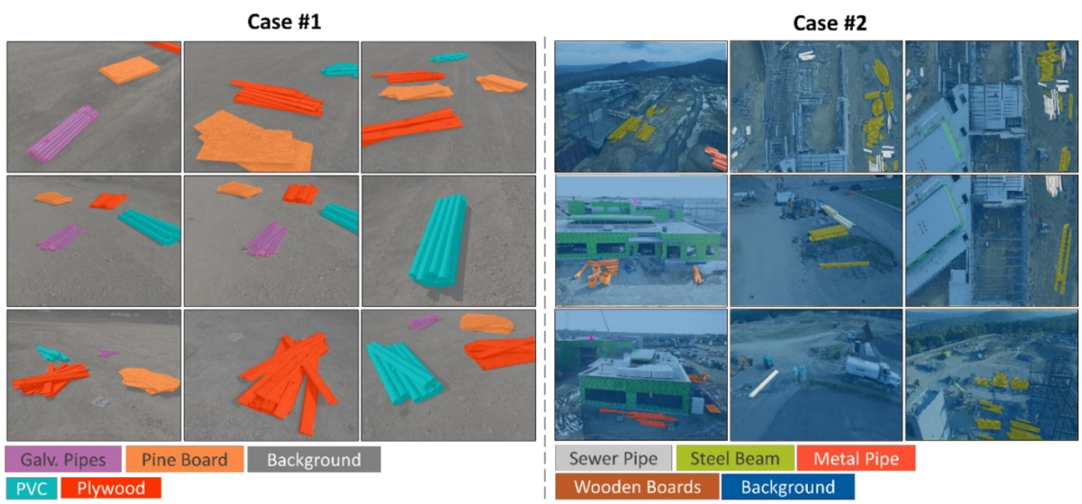

Figure 10. Examples of manually annotated images in case studies

Alexnet has two parallel convolutional neural networks connected via cross-connections [82]. To increase accuracy in deep learning models, the Vgg networks are leveraged, which contain large numbers of parameters. Although the Vgg networks are computationally expensive to be optimized due to a higher number of parameters, they are generally used as a baseline for feature extraction [85]. Finally, to enhance the efficiency of the parameter optimization and reduce the search space, residual networks such as Resnet18 and Resnet50 are leveraged, which has demonstrated high performance in terms of computation and accuracy [84]. Unlike conventional networks, the Resnet architectures are robust for optimization, and the performance of the network is enhanced upon increasing layers of the network [84]. The attributes, as well as the averaged accuracy of the semantic segmentation of each deep neural network in the case study of a residential construction site are summarized in Table 2.

Table 2. Performance of convolutional deep neural networks

Networks	Depth (layers)	Parameters (millions)	Averaged accuracy (%)
Alexnet	8	61.0	89.1
Vgg19	19	144.0	92.3
Resnet18	50	11.4	98.1
Resnet 50	101	25.6	98.2

As a proof of concept, in our case studies, we built upon the Resnet50 model to carry out the semantic segmentation. Figure 11 demonstrates the confusion matrix obtained to measure the 2D semantic segmentation accuracy in case studies.

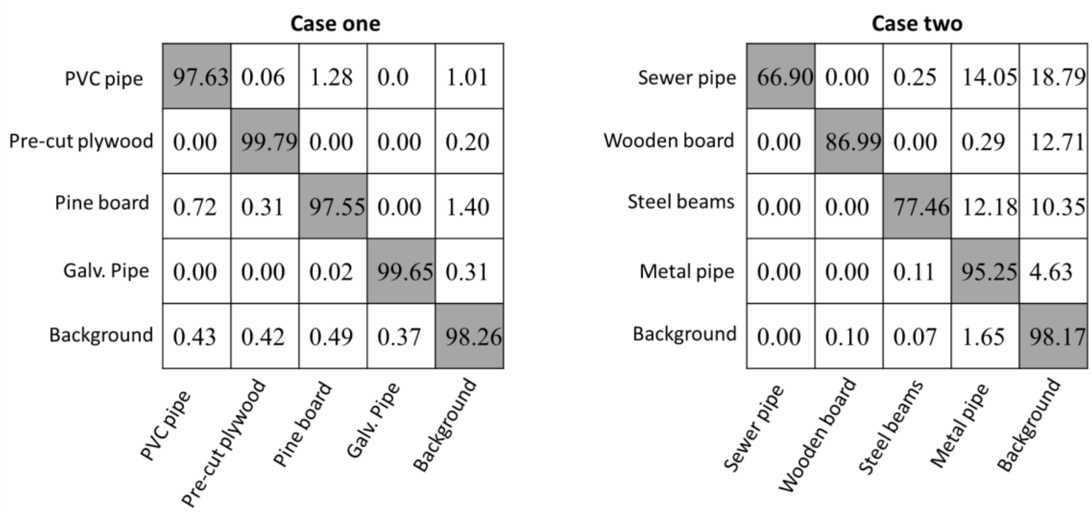

Figure 11. Confusion matrix over testing dataset for segmentation

4.2.2. Instance segmentation of PWDs

By leveraging the images presented in our case studies, a dense point cloud is reconstructed, and the associated depth map for each image is obtained. The depth-aware projection of the semantic information onto the point cloud model is then conducted, and the point cloud is semantically segmented. The oriented bounding boxes are enforced to demonstrate PWDs in the resulting digital twin model in the form of point clouds. Points enclosed in each bounding box are trimmed from the rest of the point clouds, and the associated PWD is further explored through the volumetric measurement and the threat assessment. Examples of point cloud models and their segmentation as well as the outcome of the instance segmentation, are presented in Figure 12.

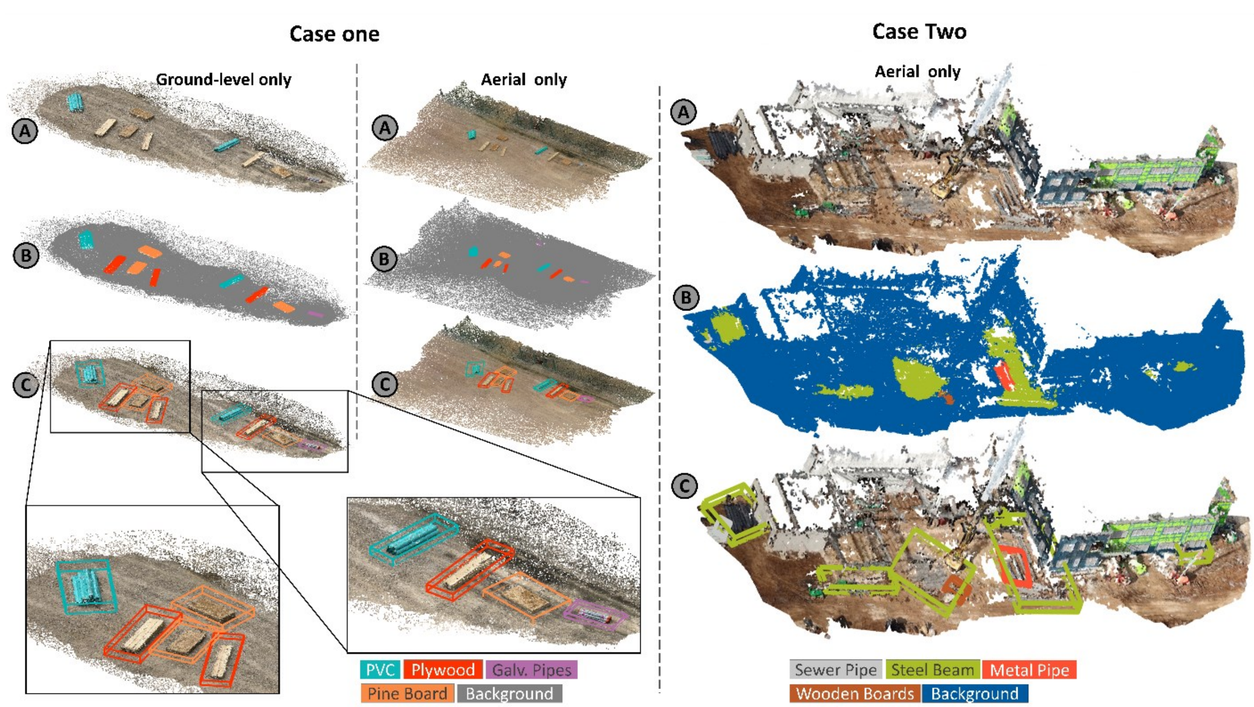

Figure 12. (a) original point cloud, (b) segmented point cloud, and (c) the instance segmentation of PWDs in case studies

4.2.3. Volumetric measurement

The outcomes of the volumetric measurements on nine instances of PWDs are compared against the ground truth, and the error is obtained per instance. The grid size of discretization was experimentally set to 3 centimeters as a proof of concept, in the light of required computational cost as the computing time could be in inverse proportion to the grid sizing as shown in [71]. Table 3 shows the error of the volumetric measurement based on segmented point cloud models of a residential construction site in the case study.

Table 3. Volumetric measurement on PWDs based on segmented point cloud models

Pile ID#	**PWDs**	**Measured Volume ($\mathbf{cm^3}$)**	**Ground Truth ($\mathbf{cm^3}$)**	**Error (%)**
1	PVC pipe	168,302	164,329	2.4
2	Plywood	112,773	105,768	6.6
3	Pine board	109,720	102,564	6.9
4	Pine board	70,916	68,376	3.7
5	Plywood	38,521	35,256	9.2
6	PVC pipe	80,803	74,695	8.1
7	Plywood	72,709	70,512	3.1
8	Pine board	53,410	51,270	4.1
9	Galv. Pipe	20,065	18,902	6.1

4.2.4. Heatmaps based on the threats associated with PWDs

The unit mass per volume ($\boldsymbol{\rho}_{pwd}$) is built upon to obtain the mass of each pile based on the volume. The plywood, pine board, and wooden board are considered plate-type debris, while PVC and sewer pipe, steel beam, and galvanized pipe are classified as rod-type debris. The critical wind speed of PWDs is calculated through Equations (5) and (6). Material properties such as mass per unit volume of materials were built upon [86,87]. Threats associated with PWDs are then assessed based on the mass of debris, wind speed, and the critical wind speed of debris, in terms of the kinetic energy. Figure 13 illustrates examples of heatmaps with different wind speeds. The wind speeds of 42, 58, 70, and 100m/s correspond to hurricane categories one, three, four, and five, based on the Saffir-Simpson scale [88].

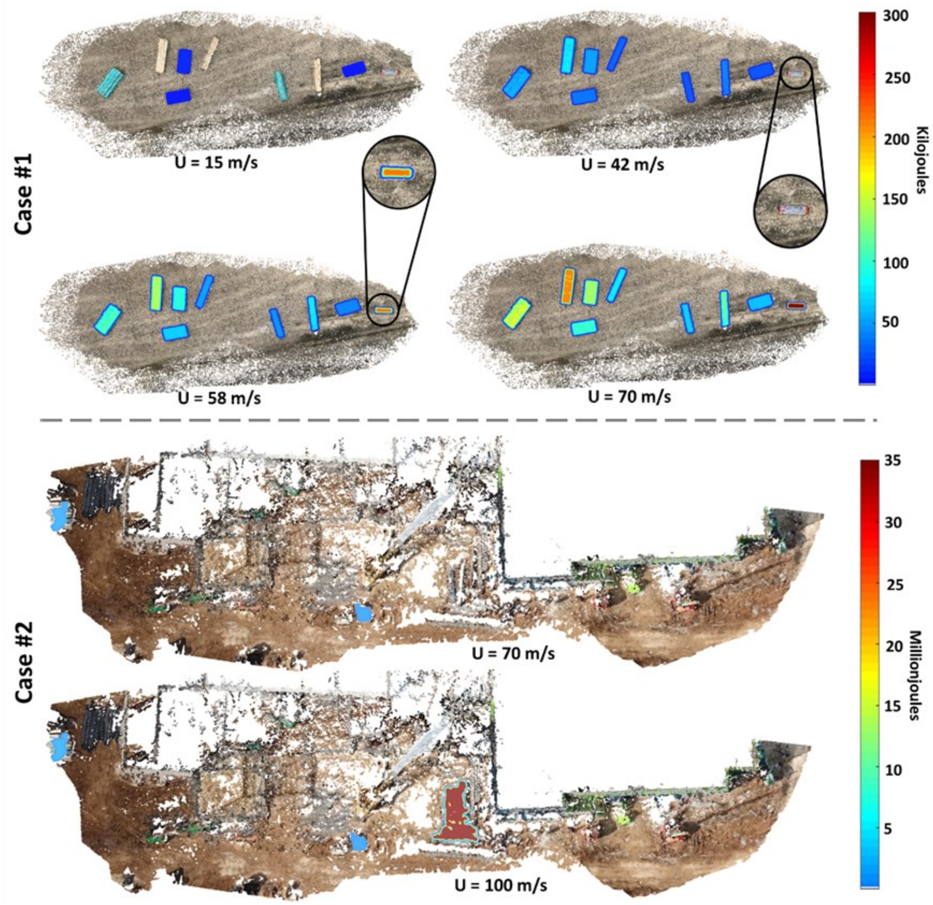

Figure 13. Examples of kinetic energy-based threat assessment of PWDs at the different intensity of winds

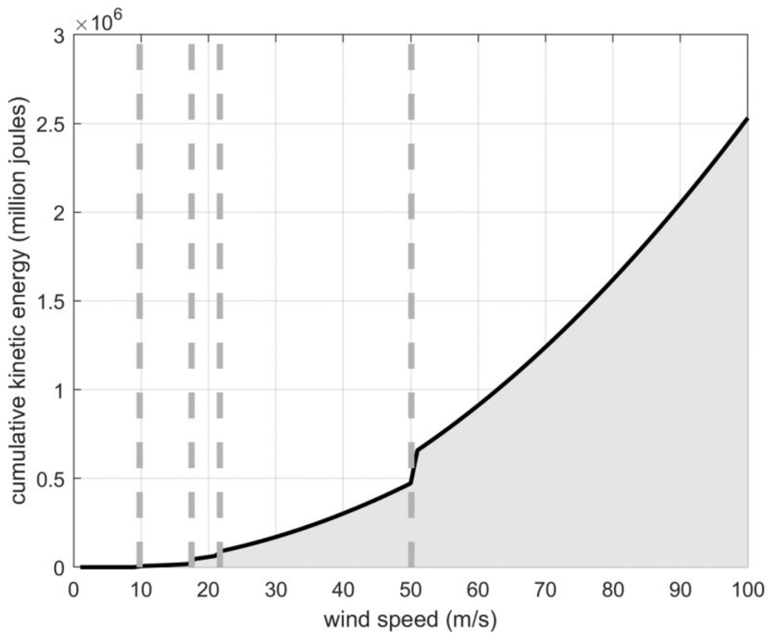

Figure 14. Cumulative kinetic energy associated with PWDs with respect to different intensity of winds

Figure 14 demonstrates the cumulative kinetic energy with respect to PWDs that are present in the case study of a residential construction site. In our case study, the critical wind speeds of 9.8, 17.5, 21.7, and 50.1 m/s are noted for pine board, plywood, PVC pipe, and galvanized pipe, respectively. As observed, the cumulative kinetic energy demonstrates a gradual increase at lower wind speeds but sharply escalates at higher intensity of winds. In addition, an increase in released energy level is observed at the proximity of critical wind speeds, as PWDs become airborne. In the case studies, around 35 percent of an increase was observed at 50.1 m/s as galvanized pipe becomes airborne. Such a significant change in kinetic energy is relevant to the higher density (i.e., high threats) of galvanized pipe compared to the rest of PWDs presented in the case studies.

5. Discussions

Figure 13 illustrates the threats associated with PWDs over the at-risk construction environment with respect to the wind intensity. The advantages of generating a heatmap to delineate the threat could be perceived on two fronts: 1) depending on the critical wind speed, some PWDs do not pose any threat at lower wind speeds. For example, in case #1, at 15m/s of winds, it was observed that only pine boards in our case studies are identified as a potential threat among the rest of PWDs. This implies that for lower wind intensities, the hurricane preparedness checklist could be streamlined, which requires securing/relocating the corresponding PWDs from jobsites, and at the same time, relaxing preparedness ordinances for the rest of PWDs that are present in the scene.

Such an abstract and yet focused preparedness plan could be effective, given that there is a limited resource (i.e., time, manpower) for hurricane preparedness. 2) Given a particular wind speed, the level of threats among PWDs may vary, which can help the prioritization for preparedness. For instance, at 70m/s of wind speed, galvanized pipe is flagged as the most hazardous PWD in our case studies, while pine boards present a less threat in the jobsite. In our case studies, the volume of galvanized pipes accounts for around three percent of the entire volume of PWDs presented. However, as demonstrated in Figure 14, such a small portion of PWDs could have a significant threat once they become airborne. In this regard, at a given wind speed, exploring the level of potential threat among the PWDs can provide useful information for planning preparedness. Visualization of threat through heatmaps helps provide a prioritized plan to secure PWDs and sorts the most hazardous PWDs to the least. Identifying and prioritizing preemptive measures with respect to the risk level of PWDs is expected to support risk-informed decision-makings for implementing construction site emergency operating protocols to prepare for extreme wind events in an effective manner.

In this paper, the depth-aware projection framework could enhance the performance of the point cloud segmentation, which is the critical step to assess the threat associated with PWDs. Depth information indicates the distance in which semantic projection from image to point cloud is valid, in order to account for occlusions during projections. Here, we demonstrate the performance enhancement gained through the depth-aware projection versus the baseline projection through Equation (1). The outcome of the depth-aware projection is shown in Figure 15a, and the baseline projection is shown in Figure 15b. Correctly classified and misclassified points are shown in Figure 15c. The average accuracy of the baseline projection was 97.85 percent, while the proposed depth-aware projection demonstrates the accuracy of 99.8 percent in 3D semantic segmentation in our case studies.

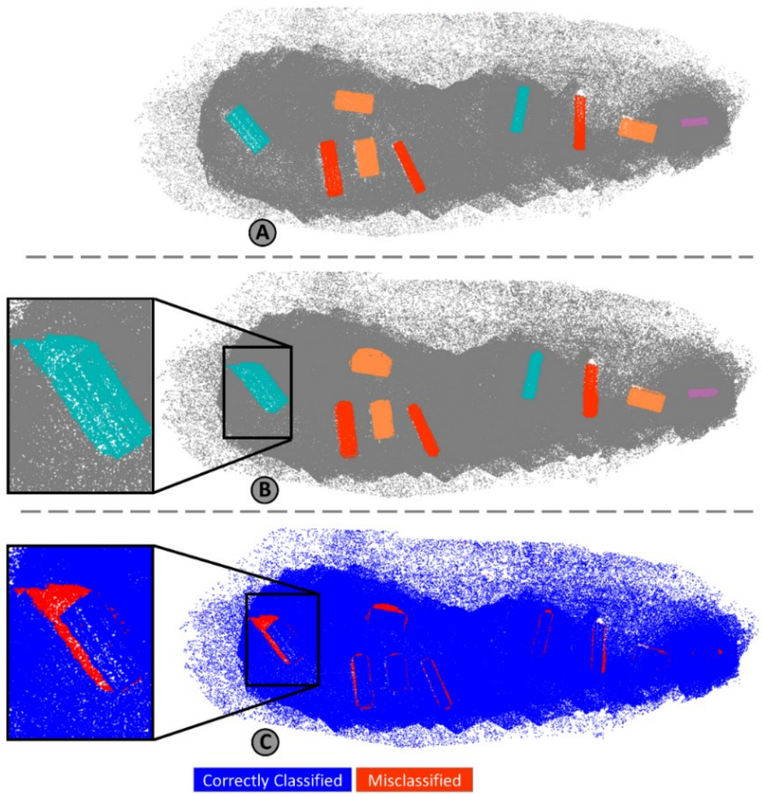

Figure 15. (a) the proposed depth-aware projection, (b) the baseline projection, and (c) the classification confusion of (b)

Although OSHA recommends pile and pallet items to be neatly stacked up to ensure stability and enable self-supporting [89], there often exist unstacked piles in jobsites. The proposed volumetric measurement performed well, but a lower accuracy was observed among relatively unstacked piles due to higher levels of disorganization. The overestimation on volumetric measurements often happened due to large amounts of empty spaces within unstacked piles. In this regard, we acknowledge that the volumetric measurement on unstacked piles could be an underlying challenge in vision-based approach as a RGB camera cannot see the unseen inside material piles. In order to estimate the volume taking account of empty spaces, a level of disorganization could be analyzed to consider a lower density of unstacked piles. However, it is expected that unstacked piles demonstrate a wide range of disorganization as the level of disarrangement in stacking varies among piles. Building on [90], the level of disarrangement in stacks could be investigated. First, a target object could be isolated through the semantic segmentation (Figure 16a). Edges are detected to keep dominant edges in the image through thresholding over gradients (Figure 16b) [91]. Then dominant straight lines are extracted through the Hough transformation (Figure 16c) [92]. Finally, the orientations of straight lines are investigated, and a histogram of line orientation can be generated. As observed in Figure 16d, for stacked PWDs, the standard deviation of line orientation is lower compared to that of relatively unstacked PWDs. The standard deviation of line orientation could represent the level of disorganization in stacking. Such level of disorganization among relatively unstacked piles would be further studied to calibrate the volumetric measurement. But in case of relatively unstacked piles, it is noted that they should be considered with the top priority for hurricane preparedness, and thus the detection of such objects based on the level of disorganization and their localization through the digital twinning module could be sufficient to trigger the prioritized actions (i.e., quick relocations) before extreme wind events.

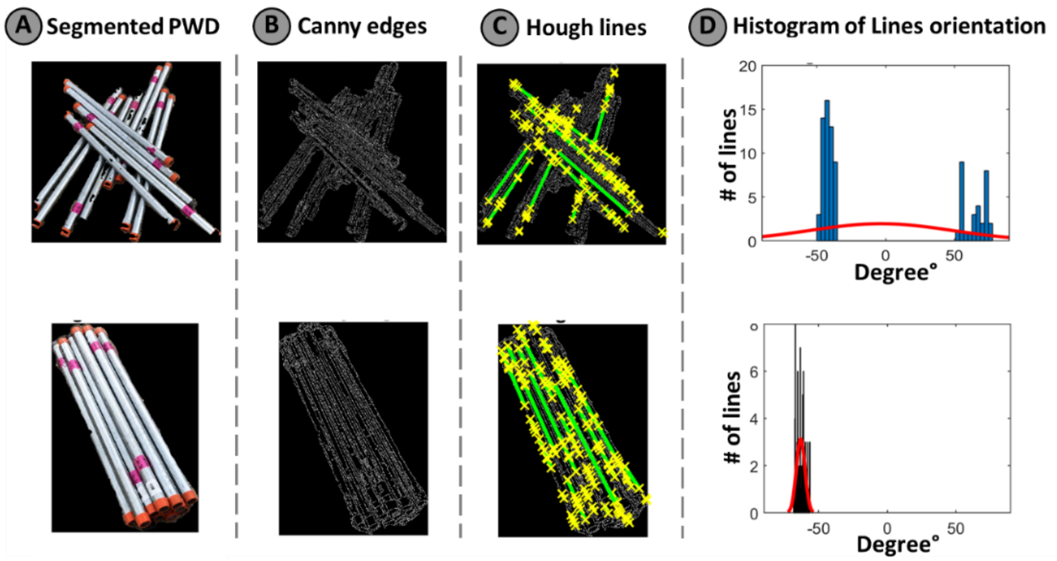

Figure 16. Level of disarrangement among relatively unstacked piles (top) and stacked piles (bottom)

6. Conclusions

Potential wind-borne debris (PWDs) are among the most destructive elements in extreme wind events. In particular, construction sites containing unsecured resources are identified among the most exposed and undefended environments to extreme wind events. Thus far, preemptive efforts have been put in by construction firms to develop and implement protocols to identify PWDs and mitigation plans to better prepare against wind events. However, the assessment is not systematic, and heuristic approaches in jobsites are likely to be error-prone and labor-intensive. The advancement of machine vision and the convenience of UAVs have offered opportunities to collect large-scale imagery and generate digital photologs to keep the record of errands in construction projects. In this paper, we propose a rapid and in-situ risk assessment of PWDs by encoding their risk into machine vision algorithms to automatically flag the degree of vulnerability in jobsites. The proposed method is built upon three modules: 1) digital twining and rapid 2D/3D semantic segmentation, 2) volumetric measurement and the mass evaluation, and 3) risk assessment on PWDs. The proposed method generates site-specific heatmaps regarding threats that is respective to the intensity of wind events. PWDs presented in our case studies are commonly found in residential construction sites, including plywoods, pine boards, or PVC/galvanized pipes. The proposed method supports risk-informed decision-making by providing a heads-up to practitioners and fosters awareness of the ways in which hurricanes could be destructive in construction sites. Moreover, the proposed method has the potential in rapid scene understanding to be integrated into site monitoring systems. While this research enables an automated risk assessment in the context of hurricane preparedness, there are open research challenges associated with the proposed method. For instance, it is expected that 3D and 2D semantic segmentation modules may demonstrate poor performance in suboptimal weather conditions such as rainy [93] and foggy [94] situations or dim light conditions [95]. Moreover, the presence of occlusions and moving objects in jobsites is another challenge in reality-capture and digital twining frameworks. In this regard, building a robust machine vision-based system that can account for such challenges is the direction of our ongoing research.

Acknowledgment

This material is based upon work supported by the National Science Foundation under Grant No. 1832187. Any opinions, findings, and conclusions or recommendations expressed in this material are those of the author(s) and do not necessarily reflect the views of the National Science Foundation.

References

[1] Y. Ham, S.J. Lee, A.G. Chowdhury, Imaging-to-simulation framework for improving disaster preparedness of construction projects and neighboring communities, Computing in Civil Engineering 2017, 2017, pp. 230-237 DOI: https://doi.org/10.1061/9780784480830.029.

[2] M.S. CHAVEZ, Hurricane Preparedness in a Construction Site: a Framework to Assess the Construction Companies' Current Practices, (2016) DOI: https://10.25148/etd.FIDC001187

[3] A. Gupta, H. Lamba, P. Kumaraguru, A. Joshi, Faking sandy: characterizing and identifying fake images on twitter during hurricane sandy, Proceedings of the 22nd international conference on World Wide Web, 2013, pp. 729-736 DOI: https://doi.org/10.1145/2487788.2488033.

[4] Fermino, Sandy caused $185M in damage to WTC site, (2013).

[5] P. McCarthy, E. Soderberg, A. Dix, Wind damage to dockside cranes: Recent failures and recommendations, TCLEE 2009: Lifeline Earthquake Engineering in a Multihazard Environment, 2009, pp. 1-12 DOI: https://doi.org/10.1061/41050(357)50.

[6] Y. Li, B.R. Ellingwood, Hurricane damage to residential construction in the US: Importance of uncertainty modeling in risk assessment, Engineering structures 28 (2006) 1009-1018 DOI: https://doi.org/10.1016/j.engstruct.2005.11.005.

[7] D.L. Bass, G. Overcash, FEMA's Wind Retrofit Guide, Advances in Hurricane Engineering: Learning from Our Past, 2013, pp. 229-237 DOI: https://doi.org/10.1061/9780784412626.021.

[8] J. Zhu, A. Mostafavi, An Integrated Framework for the Assessment of the Impacts of Uncertainty in Construction Projects Using Dynamic Network Simulation, Computing in Civil Engineering 2015, 2015, pp. 355-362 DOI: https://doi.org/10.1061/9780784479247.044.

[9] B. Lee, Engineering design for extreme winds in Hong Kong, Hong Kong Engineer 16 (4) (1988) 15-23 DOI: https://ci.nii.ac.jp/naid/10007252645/.

[10] J.E. Minor, Windborne debris and the building envelope, Journal of Wind Engineering and Industrial Aerodynamics 53 (1-2) (1994) 207-227 DOI: https://doi.org/10.1016/0167-6105(94)90027-2.

[11] A. Kareem, Performance of cladding in Hurricane Alicia, Journal of Structural Engineering 112 (12) (1986) 2679-2693 DOI: https://doi.org/10.1061/(ASCE)0733-9445(1986)112:12(2679).

[12] F. Kadri, B. Birregah, E. Châtelet, The impact of natural disasters on critical infrastructures: A domino effect-based study, Journal of Homeland Security and Emergency Management 11 (2) (2014) 217-241 DOI: https://doi.org/10.1515/jhsem-2012-0077.

[13] WKBW News, Wind Damage to Construction Site, https://www.youtube.com/watch?v=v-3c4CFLtvY, Access Date: 10/13/21.

[14] NBC2 News, Construction sites bracing for Hurricane Dorian's impact, https://www.youtube.com/watch?v=uM5yGAKMUjQ, Access Date: 10/13/21.

[15] SunSentinel, Hurricane Irma debris piles could be around for months, https://www.sun-sentinel.com/news/weather/hurricane/fl-reg-hurricane-irma-debris-disposal-delays-20170919-story.html, Access date: 10/13/21.

[16] United States Department of Homeland Security, Homeland SPre-Disaster Debris Removal Contracts in Florida, https://www.oig.dhs.gov/sites/default/files/assets/2020-08/OIG-20-44-Jul20.pdf, Access Date: 10/13/21.

[17] S.A. Cauffman, Performance of physical structures in Hurricane Katrina & Hurricane Rita: A reconnaissance report, DIANE Publishing, 2006 DOI: https://doi.org/10.6028/nist.tn.1476.

[18] I. Jeelani, K. Asadi, H. Ramshankar, K. Han, A. Albert, Real-world Mapping of Gaze Fixations Using Instance Segmentation for Road Construction Safety Applications, (2019) DOI: https://arxiv.org/abs/1901.11078.

[19] M. Kamari, O. Gunes, Segmentation and Analysis of a Sketched Truss Frame Using Morphological Image Processing Techniques, (2016) DOI: https://arxiv.org/ftp/arxiv/papers/2009/2009.13144.pdf.

[20] Y. Ham, M. Kamari, Automated content-based filtering for enhanced vision-based documentation in construction toward exploiting big visual data from drones, AutoCon (2019) DOI: https://doi.org/10.1016/j.autcon.2019.102831.

[21] M. Kamari, Y. Ham, Automated Filtering Big Visual Data from Drones for Enhanced Visual Analytics in Construction, ASCE Construction Research Congress 2018, 2018 DOI: https://doi.org/10.1061/9780784481264.039.
[22] Z. Ghorbani, A.H. Behzadan, Identification and Instance Segmentation of Oil Spills Using Deep Neural Networks, CSEE 2020 (2020).
[23] M. Razavi, H. Alikhani, V. Janfaza, B. Sadeghi, E. Alikhani, An automatic system to monitor the physical distance and face mask wearing of construction workers in covid-19 pandemic, (2021) DOI: https://arxiv.org/ftp/arxiv/papers/2101/2101.01373.pdf.
[24] M. Kamari, Y. Ham, Semantic Detection of Potential Wind-borne Debris in Construction Jobsites: Digital Twining for Hurricane Preparedness and Jobsite Safety International Conference on Computing in Civil Engineering (i3CE), ASCE, Orlando, Florida, 2021 DOI: https://doi.org/10.1061/9780784482865.097.
[25] M. Noghabaei, A. Heydarian, V. Balali, K.J.D. Han, Trend analysis on adoption of virtual and augmented reality in the architecture, engineering, and construction industry, 5 (1) (2020) 26 DOI: https://doi.org/10.3390/data5010026.
[26] M. Noghabaei, K. Asadi, K. Han, Virtual manipulation in an immersive virtual environment: Simulation of virtual assembly, Computing in Civil Engineering 2019: Visualization, Information Modeling, and Simulation, American Society of Civil Engineers Reston, VA, 2019, pp. 95-102 DOI: https://doi.org/10.1061/9780784482421.013.
[27] B. Sherafat, C.R. Ahn, R. Akhavian, Automated Methods for Activity Recognition of Construction Workers and Equipment: State-of-the-Art Review, (2020) DOI: https://doi.org/10.1061/(ASCE)CO.1943-7862.0001843.
[28] S. Siebert, J. Teizer, Mobile 3D mapping for surveying earthwork projects using an Unmanned Aerial Vehicle (UAV) system, Automation in Construction 41 (2014) DOI: https://doi.org/10.1016/j.autcon.2014.01.004.
[29] Y. Ham, K.K. Han, J.J. Lin, M. Golparvar-Fard, Visual monitoring of civil infrastructure systems via camera-equipped Unmanned Aerial Vehicles (UAVs): a review of related works, Visualization in Engineering 4 (2016) 1 DOI: https://doi.org/10.1186/s40327-015-0029-z.
[30] M. Golparvar-Fard, F. Peña-Mora, S. Savarese, Automated Progress Monitoring Using Unordered Daily Construction Photographs and IFC-Based Building Information Models, Journal of Computing in Civil Engineering 29 (2015) 04014025 DOI: https://10.1061/(ASCE)CP.1943-5487.0000205.
[31] K.K. Han, M. Golparvar-Fard, Automated Monitoring of Operation-level Construction Progress Using 4D BIM and Daily Site Photologs, Construction Research Congress 2014, American Society of Civil Engineers, Reston, VA, 2014, pp. 1033-1042 DOI: https://doi.org/10.1061/9780784413517.106.
[32] M. Golparvar-Fard, F. Peña-Mora, S. Savarese, D4AR–a 4-dimensional augmented reality model for automating construction progress monitoring data collection, processing and communication, Journal of information technology in construction 14 (13) (2009) 129-153.
[33] M. Gheisari, B. Esmaeili, Unmanned aerial systems (UAS) for construction safety applications, Construction Research Congress 2016, 2016, pp. 2642-2650 DOI: https://doi.org/10.1061/9780784479827.263.
[34] M. Gheisari, J. Irizarry, B.N. Walker, UAS4SAFETY: The potential of unmanned aerial systems for construction safety applications, Construction Research Congress 2014: Construction in a Global Network, 2014, pp. 1801-1810 DOI: https://doi.org/10.1061/9780784413517.184.
[35] J. Irizarry, M. Gheisari, B. Walker, Usability Assessment of Drone Technology as Safety Inspection Tools, Journal of information technology in construction 17 (2012) DOI: http://www.itcon.org/2012/12.
[36] B. Alizadeh, A.H.J.C. Behzadan, Environment, U. Systems, Flood depth mapping in street photos with image processing and deep neural networks, 88 (2021) 101628 DOI: https://doi.org/10.1016/j.compenvurbsys.2021.101628.

[37] B. Alizadeh, D. Li, Z. Zhang, A.H.J.a.p.a. Behzadan, Feasibility study of urban flood mapping using traffic signs for route optimization, (2021) DOI: https://arxiv.org/abs/2109.11712.
[38] M. Kamari, Y. Ham, Analyzing Potential Risk of Wind-induced Damage in Construction Sites and Neighboring Communities using Large-scale Visual Data from Drones, CRC 2020, Tempe, Arizona, 2020 DOI: https://doi.org/10.1061/9780784482865.097.
[39] C.E. Gregg, B.F. Houghton, D.M. Johnston, D. Paton, D. Swanson, The perception of volcanic risk in Kona communities from Mauna Loa and Hualālai volcanoes, Hawai, (2004) DOI: https://doi.org/10.1016/S0377-0273(03)00288-9.
[40] L.S. Pheng, B. Raphael, W.K.J.S.s. Kit, Tsunamis: some pre-emptive disaster planning and management issues for consideration by the construction industry, 24 (5) (2006) 378-396 DOI: https://doi.org/10.1108/02630800610711979.
[41] G. Carter, S.D.J.J.o.c.e. Smith, management, Safety hazard identification on construction projects, 132 (2) (2006) 197-205 DOI: https://doi.org/10.1061/(ASCE)0733-9364(2006)132:2(197).
[42] A. Albert, M.R. Hallowell, B.M.J.C.M. Kleiner, Economics, Experimental field testing of a real-time construction hazard identification and transmission technique, 32 (10) (2014) 1000-1016 DOI: https://doi.org/10.1080/01446193.2014.929721.
[43] D. Paton, D.J.D.P. Johnston, M.A.I. Journal, Disasters and communities: vulnerability, resilience and preparedness, (2001) DOI: https://doi.org/10.1108/EUM0000000005930.
[44] B. Adame, C.H.J.D.P. Miller, Management, Vested interest: developing scales for assessing flooding preparedness, (2016) DOI: https://doi.org/10.1108/DPM-08-2015-0196.
[45] S. Asadi, E. Karan, A.J.I.J.o.S. Mohammadpour, Advancing safety by in-depth assessment of workers attention and perception, 1 (03) (2017) 46-60 DOI: 10.24900/ijss/01034660.2017.1201.
[46] R.-J. Dzeng, C.-T. Lin, Y.-C.J.S.s. Fang, Using eye-tracker to compare search patterns between experienced and novice workers for site hazard identification, 82 (2016) 56-67 DOI: https://doi.org/10.1016/j.ssci.2015.08.008.
[47] S. Hasanzadeh, B. Esmaeili, M.D.J.J.o.c.e. Dodd, management, Impact of construction workers' hazard identification skills on their visual attention, 143 (10) (2017) 04017070 DOI: https://doi.org/10.1061/(ASCE)CO.1943-7862.0001373.
[48] I. Jeelani, K. Han, A.J.A.i.C. Albert, Automating and scaling personalized safety training using eye-tracking data, 93 (2018) 63-77 DOI: https://doi.org/10.1016/j.autcon.2018.05.006.
[49] I. Jeelani, A. Albert, K. Han, R.J.J.o.c.e. Azevedo, management, Are visual search patterns predictive of hazard recognition performance? Empirical investigation using eye-tracking technology, 145 (1) (2019) 04018115 DOI: https://doi.org/10.1061/(ASCE)CO.1943-7862.0001589.
[50] J. Wills, B. Lee, T. Wyatt, A model of wind-borne debris damage, Journal of Wind Engineering and Industrial Aerodynamics 90 (4-5) (2002) 555-565.
[51] J. Holmes, C.W. Letchford, N. Lin, Investigations of plate-type windborne debris—Part II: Computed trajectories, Journal of Wind Engineering and Industrial Aerodynamics 94 (1) (2006) 21-39 DOI: https://doi.org/10.1016/j.jweia.2005.10.002.
[52] J. Holmes, Trajectories of spheres in strong winds with application to wind-borne debris, Journal of Wind Engineering and Industrial Aerodynamics 92 (1) (2004) 9-22 DOI: https://doi.org/10.1016/j.jweia.2003.09.031.
[53] M.J.I.t.o.c. Liu, Robotic online path planning on point cloud, 46 (5) (2015) 1217-1228 DOI: https://10.1109/TCYB.2015.2430526.
[54] L. Han, T. Zheng, Y. Zhu, L. Xu, L.J.I.T.o.V. Fang, C. Graphics, Live Semantic 3D Perception for Immersive Augmented Reality, 26 (5) (2020) 2012-2022 DOI: https://10.1109/TVCG.2020.2973477.
[55] M. Abdou, M. Elkhateeb, I. Sobh, A.J.a.p.a. Elsallab, End-to-end 3d-pointcloud semantic segmentation for autonomous driving, (2019) DOI: https://arxiv.org/abs/1906.10964.

[56] T. Ni, L. Xie, H. Zheng, E.K. Fishman, A. Yuille, Elastic boundary projection for 3d medical imaging segmentation, (2018) DOI: https://arxiv.org/abs/1812.00518.

[57] H. Su, S. Maji, E. Kalogerakis, E. Learned-Miller, Multi-view convolutional neural networks for 3d shape recognition, Proceedings of the IEEE international conference on computer vision, 2015, pp. 945-953 DOI: https://arxiv.org/abs/1505.00880.

[58] D. Maturana, S. Scherer, Voxnet: A 3d convolutional neural network for real-time object recognition, 2015 IEEE/RSJ International Conference on Intelligent Robots and Systems (IROS), IEEE, 2015, pp. 922-928 DOI: https://10.1109/IROS.2015.7353481.

[59] M. Bassier, M. Vergauwen, F.J.R.S. Poux, Point Cloud vs. Mesh Features for Building Interior Classification, 12 (14) (2020) 2224 DOI: https://doi.org/10.3390/rs12142224.

[60] C.R. Qi, H. Su, K. Mo, L.J. Guibas, Pointnet: Deep learning on point sets for 3d classification and segmentation, Proceedings of the IEEE Conference on Computer Vision and Pattern Recognition, 2017, pp. 652-660 DOI: https://arxiv.org/abs/1612.00593.

[61] J.W. Ma, T. Czerniawski, F. Leite, Semantic segmentation of point clouds of building interiors with deep learning: Augmenting training datasets with synthetic BIM-based point clouds, Automation in Construction 113 (2020) 103144 DOI: https://doi.org/10.1016/j.autcon.2020.103144.

[62] E. Valero, F. Bosché, A.J.A.i.C. Forster, Automatic segmentation of 3D point clouds of rubble masonry walls, and its application to building surveying, repair and maintenance, 96 (2018) 29-39 DOI: https://doi.org/10.1016/j.autcon.2018.08.018.

[63] A. Khaloo, D.J.A.E.I. Lattanzi, Robust normal estimation and region growing segmentation of infrastructure 3D point cloud models, 34 (2017) 1-16 DOI: https://doi.org/10.1016/j.aei.2017.07.002.

[64] Q. Wang, Automatic checks from 3D point cloud data for safety regulation compliance for scaffold work platforms, Automation in Construction 104 (2019) 38-51 DOI: https://doi.org/10.1016/j.autcon.2019.04.008.

[65] Q. Wang, M.-K.J.A.E.I. Kim, Applications of 3D point cloud data in the construction industry: A fifteen-year review from 2004 to 2018, 39 (2019) 306-319 DOI: https://doi.org/10.1016/j.aei.2019.02.007.

[66] Y. Xu, S. Tuttas, L. Hoegner, U.J.A.i.C. Stilla, Reconstruction of scaffolds from a photogrammetric point cloud of construction sites using a novel 3D local feature descriptor, 85 (2018) 76-95 DOI: https://doi.org/10.1016/j.autcon.2017.09.014.

[67] C. Kim, H. Son, C.J.A.i.C. Kim, Automated construction progress measurement using a 4D building information model and 3D data, 31 (2013) 75-82 DOI: https://doi.org/10.1016/j.autcon.2012.11.041.

[68] Q. Wang, J.C. Cheng, H.J.C.A.C. Sohn, I. Engineering, Automated estimation of reinforced precast concrete rebar positions using colored laser scan data, 32 (9) (2017) 787-802 DOI: https://doi.org/10.1111/mice.12293.

[69] J. Chen, Y. Fang, Y.K. Cho, C.J.J.o.C.i.C.E. Kim, Principal axes descriptor for automated construction-equipment classification from point clouds, 31 (2) (2017) 04016058 DOI: https://doi.org/10.1061/(ASCE)CP.1943-5487.0000628.

[70] S.I. Nikolenko, Synthetic data for deep learning, Springer, 2019.

[71] M. Kamari, Y. Ham, Vision-based volumetric measurements via deep learning-based point cloud segmentation for material management in jobsites, Automation in Construction (2020) DOI: https://doi.org/10.1016/j.autcon.2018.08.018.

[72] R. Lu, I. Brilakis, Digital twinning of existing reinforced concrete bridges from labelled point clusters, Automation in Construction 105 (2019) 102837 DOI: https://doi.org/10.1016/j.autcon.2019.102837.

[73] C. Wu, Towards linear-time incremental structure from motion, 2013 International Conference on 3D Vision-3DV 2013, 2013, pp. 127-134 DOI: https://doi.org/10.1109/3DV.2013.25.

[74] Y. Furukawa, J. Ponce, Accurate, Dense, and Robust Multiview Stereopsis, IEEE transactions on pattern analysis and machine intelligence 32 (2010) 1362-1376 DOI: https://10.0.4.85/TPAMI.2009.161.

[75] D.G. Lowe, others, Object recognition from local scale-invariant features., iccv, Vol. 99, 1999, pp. 1150-1157 DOI: https://10.1109/ICCV.1999.790410.

[76] R.J.A.f.H. Taher, General Recommendations for Improved Building Practices in Earthquake and Hurricane Prone Areas, (2010).

[77] S.o.W.-B. Debris, Wind-Borne Debris Hazards, American Society of Civil Engineers, 2018 DOI: https://doi.org/10.1061/9780784414965.

[78] V. Balali, M. Golparvar-Fard, Segmentation and recognition of roadway assets from car-mounted camera video streams using a scalable non-parametric image parsing method, Automation in Construction 49 (2015) 27-39 DOI: https://10.1016/j.autcon.2014.09.007.

[79] W. Chen, H.J.M. Hao, Design, Experimental and numerical study of composite lightweight structural insulated panel with expanded polystyrene core against windborne debris impacts, 60 (2014) 409-423 DOI: https://doi.org/10.1016/j.matdes.2014.04.038.

[80] M.A. Fischler, R.C. Bolles, Random sample consensus: a paradigm for model fitting with applications to image analysis and automated cartography, Communications of the ACM 24 (6) (1981) 381-395 DOI: https://doi.org/10.1145/358669.358692.

[81] A.T. Duchowski, M.M. Price, M. Meyer, P. Orero, Aggregate gaze visualization with real-time heatmaps, Proceedings of the symposium on eye tracking research and applications, 2012, pp. 13-20 DOI: https://doi.org/10.1145/2168556.2168558.

[82] A. Krizhevsky, I. Sutskever, G.E.J.C.o.t.A. Hinton, Imagenet classification with deep convolutional neural networks, 60 (6) (2017) 84-90 DOI: https://doi.org/10.1145/3065386.

[83] O. Russakovsky, J. Deng, H. Su, J. Krause, S. Satheesh, S. Ma, Z. Huang, A. Karpathy, A. Khosla, M.J.I.j.o.c.v. Bernstein, Imagenet large scale visual recognition challenge, 115 (3) (2015) 211-252 DOI: https://doi.org/10.1007/s11263-015-0816-y.

[84] K. He, X. Zhang, S. Ren, J. Sun, Deep residual learning for image recognition, Proceedings of the IEEE conference on computer vision and pattern recognition, 2016, pp. 770-778 DOI: https://10.1109/CVPR.2016.90.

[85] X. Lu, X. Duan, X. Mao, Y. Li, X.J.M.P.i.E. Zhang, Feature extraction and fusion using deep convolutional neural networks for face detection, 2017 (2017) DOI: https://doi.org/10.1155/2017/1376726.

[86] Density of Some Common Building Materials, https://www.rfcafe.com/references/general/density-building-materials.htm, Access Date: 10/23/21.

[87] PVC Datasheet, https://www.piping-designer.com/index.php/datasheets/piping-datasheets/1663-pipe-pvc-ansi-sch-120-in, Access Date: 10/23/21.

[88] H.T. Taylor, B. Ward, M. Willis, W. Zaleski, The Saffir-Simpson hurricane wind scale, Atmospheric Administration: Washington (2010) DOI: https://doi.org/10.7560/319727-010.

[89] OSHA, DOI: https://www.osha.gov/sites/default/files/publications/osha2236.pdf.

[90] J. Kim, M. Kamari, S. Lee, Y. Ham, Large Scale Visual Data-Driven Probabilistic Risk Assessment of Utility Poles regarding the Vulnerability of Power Distribution Infrastructure System, Journal of Construction Engineering and Management (2021) DOI: https://doi.org/10.1061/(ASCE)CO.1943-7862.0002153.

[91] J.J.I.T.o.p.a. Canny, m. intelligence, A computational approach to edge detection, (6) (1986) 679-698 DOI: https://10.1109/TPAMI.1986.4767851.

[92] D. Montero, C. Rueda, Detection of palm oil bud rot employing artificial vision, IOP Conference Series: Materials Science and Engineering, Vol. 437, IOP Publishing, 2018, p. 012004 DOI: https://10.1088/1757-899X/437/1/012004.

[93] H. Porav, T. Bruls, P. Newman, I can see clearly now: Image restoration via de-raining, 2019 International Conference on Robotics and Automation (ICRA), IEEE, 2019, pp. 7087-7093 DOI: https://10.1109/ICRA.2019.8793486.

[94] M. Hahner, D. Dai, C. Sakaridis, J.-N. Zaech, L. Van Gool, Semantic understanding of foggy scenes with purely synthetic data, 2019 IEEE Intelligent Transportation Systems Conference (ITSC), IEEE, 2019, pp. 3675-3681 DOI: https://arxiv.org/pdf/1910.03997.pdf.

[95] M. Limmer, J. Forster, D. Baudach, F. Schüle, R. Schweiger, H.P. Lensch, Robust deep-learning-based road-prediction for augmented reality navigation systems at night, 2016 IEEE 19th International Conference on Intelligent Transportation Systems (ITSC), IEEE, 2016, pp. 1888-1895 DOI: https://10.1109/ITSC.2016.7795862.